MIT Open Access Articles

A Through-Dielectric Radar Imaging System

Massachusetts Institute of Technology

A Through-Dielectric Radar Imaging System

Gregory L. Charvat, *Member, IEEE*, Leo C. Kempel, *Fellow, IEEE*, Edward J. Rothwell, *Fellow, IEEE*,
Christopher M. Coleman, *Member, IEEE*, and Eric L. Mokole, *Senior Member, IEEE*

Abstract—Through-lossy-slab radar imaging will be shown at stand-off ranges using a low-power, ultrawideband (UWB), frequency modulated continuous wave (FMCW) radar system. FMCW is desirable for through-slab applications because of the signal gain resulting from pulse compression of long transmit pulses (1.926–4.069 GHz chirp in 10 ms). The difficulty in utilizing FMCW radar for this application is that the air-slab boundary dominates the scattered return from the target scene and limits the upper bound of the receiver dynamic range, reducing sensitivity for targets behind the slab. A method of range-gating out the air-slab boundary by significant band-limiting of the IF stages facilitates imaging of low radar cross section (RCS) targets behind the slab. This sensor is combined with a 1D linear rail and utilized as a rail synthetic aperture radar (SAR) imaging system. A 2D model of a slab and cylinder shows that image blurring due to the slab is negligible when the SAR is located at a stand-off range of 6 m or greater, and thus, the two-way attenuation due to wave propagation through the slab is the greatest challenge at stand-off ranges when the air-slab boundary is range-gated out of the scattered return. Measurements agree with the model, and also show that this radar is capable of imaging target scenes of cylinders and rods 15.24 cm in height and 0.95 cm in diameter behind a 10 cm thick lossy dielectric slab. Further, this system is capable of imaging free-space target scenes with transmit power as low as 5 pW, providing capability for RCS measurement.

Index Terms—Dielectric slab, frequency modulated continuous wave (FMCW), linear FM, linear frequency modulation (LFM), low-power radar, pulse compresion, radar imaging, rail SAR, synthetic aperture radar, through lossy-dielectric slab imaging, ultrawideband radar.

I. INTRODUCTION

A RADAR sensor capable of imaging targets behind a lossy dielectric slab at stand-off ranges will be shown in this paper. The motivation is to develop a sensor capable of locating targets behind a lossy dielectric slab (such as concrete, plastic, wood, ceramic, drywall, or other dielectrics) without *a priori* information or assumptions about the target scene. Linear frequency modulation (LFM) radar was chosen because of the

single-pulse sensitivity and dynamic range resulting from pulse compression of long time duration (10 ms) pulses. A 10 ms pulse time is too long for use in a pulsed radar in a through-slab application because the range swath is small (typically spanning 0 to 20 m or less down range) compared to the pulse length. As a result, FMCW must be utilized, where the radar transmits and receives simultaneously. Unfortunately, the scattering off of the air-slab boundary causes the greatest target return, setting the upper bound of the dynamic range in the digital radar receiver which effectively limits sensitivity. It is for this reason that the majority of through-slab radar development has focused on UWB short-pulse radar systems, where the air-slab boundary can be range-gated out in the time domain, allowing for maximum dynamic range and sensitivity to be applied to the range bins behind the air-slab boundary. Examples of this operating in the 1–3 GHz frequency range are treated in [1]–[5]. In order to achieve the average power necessary for reasonable signal-to-noise ratios (SNRs) of returns from targets behind lossy slabs these radar systems must operate at a high peak power, or alternatively, at a low peak power with a high pulse rate frequency (PRF). Coherent integration on receive is necessary to take advantage of the increased average transmit power when operating at a high PRF. UWB short-pulse radar systems rely on the latest analog to digital converter (ADC) technology because of the bandwidths required to acquire single pulses. Motivated by ability of UWB short-pulse radar to range-gate out the air-slab boundary, but with a desire to achieve high single-pulse SNR using low peak transmit power, a modified FMCW radar architecture is developed that provides an effective range gate while at the same time operating in an FMCW mode using 10 ms LFM pulses. This architecture provides high sensitivity and dynamic range for detection of targets behind a slab with easy-to-meet ADC specifications (16 bits of resolution at 200 KSPS). This radar sensor operates at S-band, where it radiates UWB S-band linear chirps from 1.926–4.069 GHz, and it is mounted on to a 1D rail where it is utilized as a rail synthetic aperture radar (SAR) imaging sensor.

Most through-lossy-slab radar systems use some method of beam forming to localize targets behind a slab and place their antenna elements directly on or in close proximity to the slab in order to reduce air-to-slab path loss. When the antenna elements are located close to or directly on the slab the effects of Snell's law severely reduce the performance of free-space beam forming algorithms by distorting wave propagation through the slab, therefor, much research focus on through-slab beam-forming algorithms has been to develop methods to counter the Snell's law effects of the dielectric slab [6]–[11]. In this paper a 2D slab and cylinder model is developed and used to show that when SAR beamforming is utilized and the
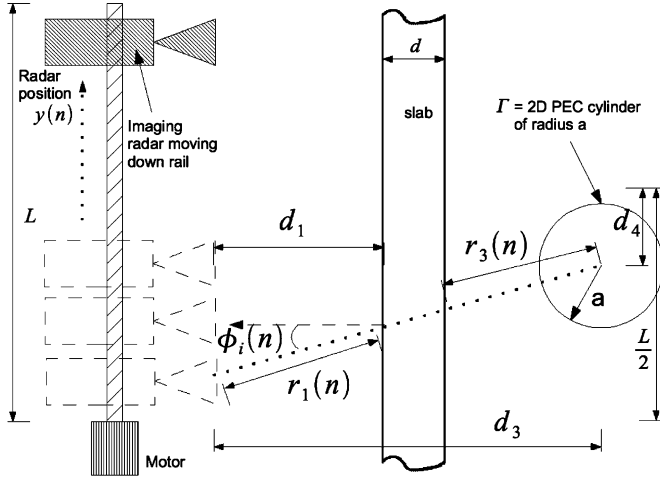
Fig. 1. Through slab imaging geometry.

imaging sensor is placed at a stand-off range (6 m or greater) very little image de-focusing occurs because the bending of the plane wave through the dielectric slab has a negligible effect on the SAR image. When range-gating is utilized the through-slab radar problem becomes one of achieving maximum sensitivity and dynamic range to overcome the stand-off distance to the slab and the two-way attenuation through the slab, rather than of re-focusing distorted radar data due to the slab, where, the single-pulse sensitivity and dynamic range of the modified FMCW architecture enables the use of this sensor at stand-off ranges.

In Sections II and III a composite 2D scattering model of a lossy slab and a cylinder is developed to demonstrate the utility of operating a through-slab SAR at stand-off ranges. Although the authors have chosen to model a 2D infinite cylinder and slab, the simulated and measured results will be shown to be in agreement. From these results, a radar architecture is developed and implemented in Section IV which provides high sensitivity due to a long duration 10 ms UWB chirp and a short-duration range gate. Free-space SAR imagery of 15.24 cm tall metal rods using 10 mW and 5 pW of peak transmit power is shown in Section V, demonstrating the high sensitivity of this design for RCS measurements. In Section VI, radar imagery through a lossy-dielectric slab is shown to agree with the model, and imagery of target scenes made up of targets as small as 15.24 cm tall metal rods behind a lossy dielectric demonstrate the SAR's sensitivity. Summary and future work are discussed in Section VII.

II. SIMULATED RANGE PROFILES

The through-slab rail SAR geometry is shown in Fig. 1, where a dielectric slab of thickness d ($= 10$ cm) is placed between the rail SAR and a perfect electric conductor (PEC) cylinder of radius a ($= 7.62$ cm). The radar system is located r_1 ($= 6.1$ m) from the front of the slab, and the cylinder is located r_3 ($= 3.05$ m) behind the slab. When simulating a range profile of this target scene it is assumed that the radar is located at a fixed location on the rail such that the angle of incidence ϕ_i ($= 0$).

The slab model is based on wave matrix theory from [12], where the normalized impedance of the dielectric with a plane wave incident at an angle of ϕ_i from the normal is

$$Z = \frac{\cos \phi_i}{\sqrt{\left(\epsilon_r + \frac{\sigma}{j\omega\epsilon_o}\right) - \sin^2 \phi_i}} \tag{1}$$

where $\epsilon_r = 5$ is the relative permittivity and the conductivity σ is assumed to be varying linearly with frequency from 0.142–0.186 S/m over the 2–4 GHz frequency range of the transmit chirp [13].

The electrical distance traveled by the wave inside of the dielectric slab d for an oblique incidence angle ϕ_i is

$$\theta = k_o d \sqrt{\left(\epsilon_r + \frac{\sigma}{j\omega\epsilon_o}\right) - \sin^2 \phi_i} \tag{2}$$

where the free-space wave number is

$$k_o = \omega\sqrt{\mu_o\epsilon_o}. \tag{3}$$

The SAR will be using vertically polarized antennas where the incident plane wave is propagating in the $\hat{x}$ direction with the electric field component in the $\hat{z}$ direction and the magnetic field component in the $-\hat{y}$ direction. Therefor the polarization is transverse magnetic to the z axis (TM^z) [14] and thus the wave amplitude coefficient c_1 at the dielectric boundary is

$$c_1 = E_o e^{-jk_o r_1} \tag{4}$$

where $r_1 = 6.1$ m is the distance from the radar system to the surface of the dielectric slab.

The simulated range-profile is calculated by solving the wave matrix equations for the complex amplitude b_1 of the field traveling in the normal direction $\hat{n}$ at the air-slab interface, which is given by

$$b_1 = \frac{c_3}{\left(1 + \frac{Z-1}{Z+1}\right)\left(1 + \frac{1-Z}{Z+1}\right)} \left[\frac{Z-1}{Z+1}e^{j\theta} + \frac{1-Z}{Z+1}e^{-j\theta} \right.$$
$$\left. + \Gamma\left(\frac{Z-1}{Z+1}\frac{1-Z}{Z+1}e^{j\theta} + e^{-j\theta}\right)\right] \tag{5}$$

where the complex amplitudes (c_1 and c_3) of the field traveling in the $-\hat{n}$ direction at the interfaces of the slab and cylinder, respectively, are related by

$$c_3 = \frac{c_1\left(1 + \frac{Z-1}{Z+1}\right)\left(1 + \frac{1-Z}{Z+1}\right)}{e^{j\theta} + \frac{Z-1}{Z+1}\frac{1-Z}{Z+1}e^{-j\theta} + \Gamma\left(\frac{1-Z}{Z+1}e^{j\theta} + \frac{Z-1}{Z+1}e^{-j\theta}\right)}. \tag{6}$$

The cylinder oriented vertically in the $\hat{z}$ direction, and thus the scattering solution Γ of a 2D PEC cylinder from [14] is given by

$$\Gamma = -e^{-j2k_o r_3} \sum_{n=0}^{\infty} (-j)^n \varepsilon_n \frac{J_n(k_o a)}{H_n^{(2)}(k_o a)} H_n^{(2)}(k_o \rho) \cos n\phi \tag{7}$$
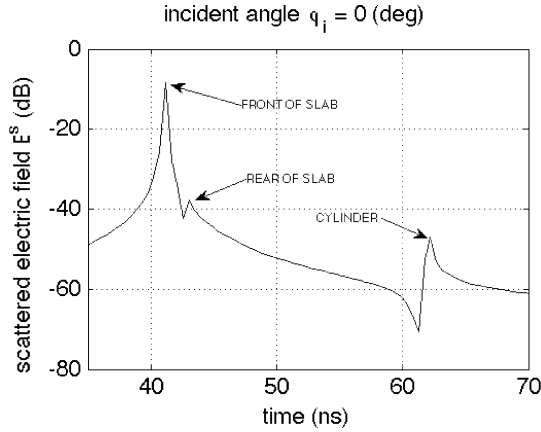
Fig. 2. Simulated range profile of a 10 cm thick lossy-dielectric slab in front a 7.62 cm radius cylinder at normal incidence.

where

$$\varepsilon_n = \begin{cases} 1 & \text{for } n = 0 \\ 2 & \text{for } n \neq 0. \end{cases}$$

Since the radar system is effectively mono-static, the bi-static observation angle ϕ is $-\pi$.

The received field, a scattered plane wave from the dielectric surface, is represented by

$$E_s = b_1 e^{-jk_o r_1}. \qquad (8)$$

The inverse discrete Fourier transform (IDFT) of E_s is taken for a number of test frequencies that emulate an S-band LFM transmitted pulse from 1.929 GHz to 4.069 GHz in 1000 steps. The incident wave amplitude $E_o = 1$. The simulated range profile shows the locations of the front of the slab at approximately 41 ns and the front of the cylinder at approximately 62 ns (Fig. 2). The scattered return off of the slab-air interface is visible at approximately 42.5 ns, where the conductivity of the slab attenuates the return off of the back side of the slab. The scattered return from the slab has the greatest magnitude in this range profile, where the cylinder behind the slab is approximately 35.8 dB below the slab.

If the PEC cylinder is placed directly behind and in close proximity to the slab, then the model breaks down because this model assumes that the scattering off of the cylinder is in the far zone. Consequently, the cylinder must be located at least 4 cylinder diameters away from the rear of the slab in order to achieve accurate results.

From these results it is clear that if the dielectric slab is not eliminated from the range profile by range-gating, then the initial reflection from the slab will set the upper bound of the dynamic range of the radar's ADC—thereby reducing the number of available bits for digitizing the returns from small targets behind the slab. In addition, it is important to have the greatest sensitivity possible to overcome the two-way attenuation due to the slab. Complex target scenes comprised of large and small scatterers behind the slab are expected in practical applications, therefore, it is important to be able to detect and image as many scatterers as possible. This can be achieved by coherent change detection (or coherent background subtraction), where dynamic

range facilitates the detection of the slightest change in scattered return from the target scene behind the slab. For these reasons a range gate, high-sensitivity, and high dynamic range are required.

III. SIMULATED SAR IMAGERY

The model from Section II is expanded, providing a simulated SAR image of a cylinder behind a lossy slab. The geometry is shown in Fig. 1. The SAR is composed of a radar sensor mounted on a linear rail of length $L = 2.44$ m. The antenna is directed toward the target scene which is made up of a dielectric slab and a 2D PEC cylinder at ranges $d_1 = 6.1$ m and $d_3 = 9.1$ m from the antenna. The cylinder location along the y axis is defined by the offset distance $d_4 (= 0)$ from the rail center $(L)/(2)$. The 2D PEC cylinder has a radius $a = 7.62$ cm and is located behind the slab. The slab has a thickness of $d = 10$ cm. The radar sensor moves down the linear rail acquiring 48 evenly spaced LFM range profiles at incremental locations $y(n)$ from $n = 1$ to 48. The incident angle ϕ_i is dependent upon the location of the radar at position $y(n)$ on the rail relative to the 2D PEC cylinder :

$$\phi_i(n) = \cos^{-1}\left[\frac{d_3}{\sqrt{\left(y(n) - \frac{L}{2} - d_4\right)^2 + d_3^2}}\right] \qquad (9)$$

where $r_1(n)$ is the distance from the radar antenna to the surface of the dielectric slab in the direction of the cylinder

$$r_1(n) = \frac{d_1}{\cos \phi_i(n)} \qquad (10)$$

and $r_3(n)$ is the distance from the opposite side of the slab to the 2D PEC cylinder

$$r_3(n) = \frac{d_3 - d_1 - d}{\cos \phi_i(n)}. \qquad (11)$$

The quantity $y(n)$ depends on the variables $\phi_i(n)$, $r_1(n)$, and $r_3(n)$, which on direct substitution into (1) through (4) yield the $y(n)$-dependent scattered field equation represented by (8).

These calculations are represented by the frequency and rail-position dependent scattered field matrix $E_s(y(n), \omega(t))$, where $y(n)$ is the cross range radar position (in m) on the linear rail shown in Fig. 1 and $\omega(t)$ is the instantaneous radial frequency at time t for an LFM modulated transmit signal:

$$\omega(t) = 2\pi\left(c_r t + f_c - \frac{BW}{2}\right). \qquad (12)$$

In this c_r is the chirp rate of 214 GHz/s, f_c is the radar center frequency of 3 GHz, and BW is the chirp bandwidth of 2.143 GHz. For the simulated imagery shown in this paper t spans 0 to 10 ms in 256 steps. The conductivity σ varies from 0.140–0.188 S/m across the transmit chirp frequency range of 1.929–4.069 GHz [13].

Coherent background subtraction is utilized in order to image the cylinder behind a lossy slab. One scattered data set was simulated without the cylinder by letting $\Gamma = 0$ represented by E_{sBack}, another was simulated with the cylinder present where
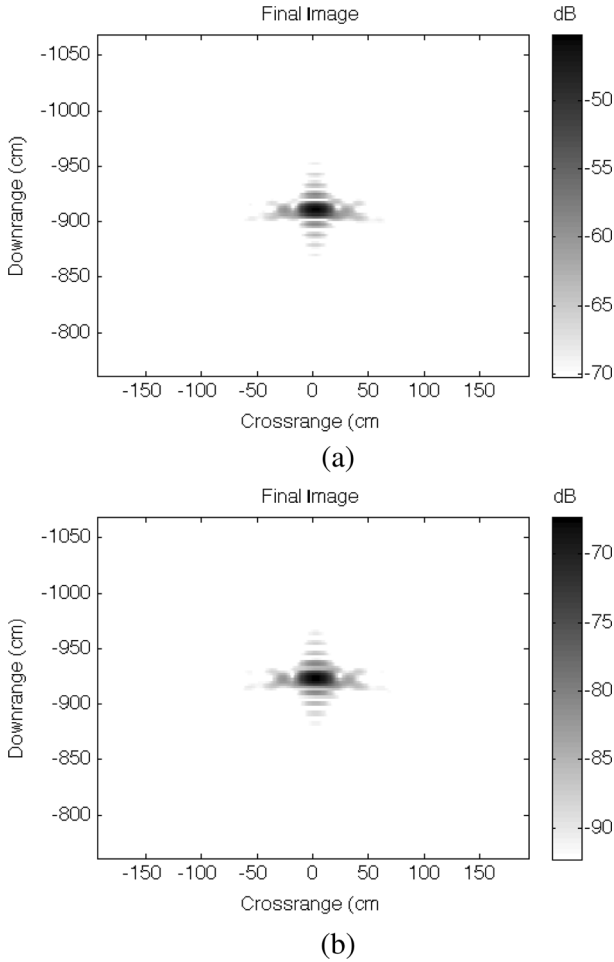
Fig. 3. Simulated SAR imagery of a 2D cylinder with radius $a = 7.62$ cm in free-space (a) and behind a 10 cm thick lossy-dielectric slab (b).

Γ is represented by (7). The difference between these two data sets is the background subtracted through slab cylinder image data set

$$E_{s\text{Targets}}(y(n),\omega(t)) = E_{s\text{Scene}}(y(n),\omega(t))$$
$$-E_{s\text{Back}}(y(n),\omega(t)). \quad (13)$$

The range migration algorithm (RMA) from [15] was used to process SAR images of this simulated data for the cylinder in free space at a range of 9.1 m and behind the lossy slab at the same range [Fig. 3(b)]. The resulting relative magnitude of the cylinder behind the dielectric slab is -67.3 dB, the down range location is -922 cm, the down range extent is approximately 8.1 cm, and the cross range extent is approximately 18.4 cm. The presence of the lossy slab does not significantly distort the SAR image; however, the intensity is greatly attenuated compared to the free-space image [Fig. 3(a)] where the relative magnitude is -45.3 dB. The resulting down range location of the cylinder in free-space is approximately -904 cm, the down range extent is 8.1 cm, and the cross range extent is approximately 17.1 cm.

These results show that the slab causes the cylinder's image to be slightly offset in downrange position. The cylinder image is not distorted noticeably because there is no change in down range extent and only a 1.3 cm increase in cross range extent. The return magnitude of the cylinder is significantly lower (-22 dB) when located behind the slab. These results indicate that a
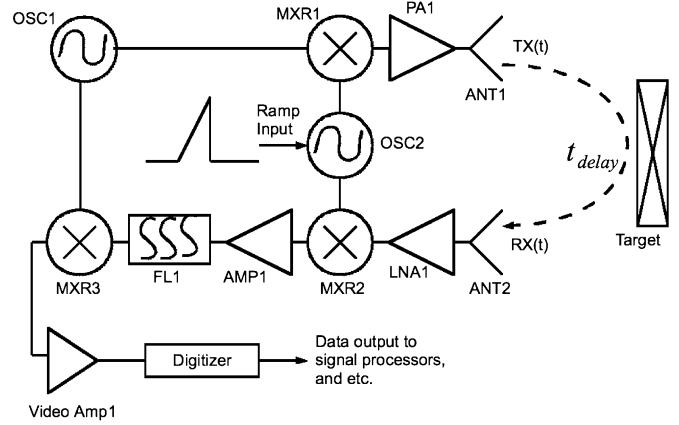

Fig. 4. Simplified block diagram of the range-gated FMCW radar system.

degradation in radar sensitivity and dynamic range appear to be the greatest challenges to imaging behind a lossy dielectric slab when the radar imaging sensor is located at a stand-off range of 6.1 m or more.

IV. SAR ARCHITECTURE

It was shown in Section II (Fig. 2) that the air-slab boundary dominates the return amplitude in a through-slab target scene. For this reason a radar architecture is developed that provides a method for range-gating out the air-wall boundary when using long-duration 10 ms transmit chirps by utilizing a modified FMCW architecture. This architecture takes advantage of the small down-range swaths inherent in practical through-slab imaging scenarios by range gating the unwanted scatterers through the use of high-Q IF band-limiting filters which are applied to the de-correlated received radar chirp. As an added benefit this method of range gating reduces the receiver noise bandwidth fed to the digitizer.

The resulting range-to-target information from a de-correlated LFM signal is in the form of low-frequency beat tones, as shown for the case of FMCW in [16], [17]. The more distant the target, the higher the frequency of the de-correlated beat tone. For this reason, it is possible to implement a short-duration range gate in a conventional FMCW radar system by simply placing a band-pass filter (BPF) at the output of the video amplifier. However, this is challenging to implement because it is difficult to design effective high circuit Q BPFs at base-band. Much higher performance BPFs are available in the form of IF communications filters centered at high frequencies which are found in two-way radios and communication receivers. Examples include crystal, ceramic, SAW, and mechanical filters.

IF filters provide a high circuit Q, where Q is the filter quality factor defined as $Q = (f_c/\text{BW})$ [18], f_c is the center frequency of the BPF, and BW is the -3 dB bandwidth of the filter. The ECS-10.7-7.5B is a 4 pole crystal filter used in this radar system that has an operating frequency f_c of 10.7 MHz with a -3 dB bandwidth BW of 7.5 kHz.

A simplified block diagram of the radar system is shown in Fig. 4. The method of range gating by using high-Q communication filters will be described in detail (in the following discussion, amplitude coefficients are ignored). OSC1 is a high frequency oscillator which is tuned just above or below the center

frequency f_c of the high-Q IF filter FL1. The frequency output of OSC1 is f_{BFO}, and the output voltage can be represented by the equation

$$\mathrm{BFO}(t) = \cos\left(2\pi f_{\mathrm{BFO}} t\right). \qquad (14)$$

The output of OSC1 is fed into the IF port of the mixer MXR1, and the local-oscillator (LO) port of MXR1 is driven by the 1.926–4.069 GHz voltage-tuned Yttrium Iron Garnet (YIG) oscillator OSC2. OSC2 is the source of the FMCW ramp modulation for this radar system. OSC2 is linear frequency modulated by a ramp input, where the output of OSC2 can be represented by the equation

$$\mathrm{LO}(t) = \cos\left(2\pi(2 \cdot 10^9 + c_r t)t\right) \qquad (15)$$

and c_r is the chirp rate in Hz/s.

OSC1 and OSC2 are mixed together in MXR1 to produce the transmit signal, which is then amplified by power amplifier PA1. The output of PA1 is fed into the transmit antenna ANT1 and radiates towards the target scene. The transmitted signal $\mathrm{TX}(t)$ from ANT1 is

$$\mathrm{TX}(t) = \mathrm{LO}(t) \cdot \mathrm{BFO}(t)$$

which after some simplification becomes

$$\mathrm{TX}(t) = \cos\left(2\pi(2 \cdot 10^9 + c_r t)t + 2\pi f_{\mathrm{BFO}} t\right) \\ + \cos\left(2\pi(2 \cdot 10^9 + c_r t)t - 2\pi f_{\mathrm{BFO}} t\right). \quad (16)$$

After propagating to the target scene, $\mathrm{TX}(t)$ scatters from the target and propagates back to the receive antenna ANT2 in the round-trip time t_{delay}. The received signal at ANT2 is represented by

$$\mathrm{RX}(t) = \cos(2\pi(2 \cdot 10^9 + c_r t)(t - t_{\mathrm{delay}}) \\ + 2\pi f_{\mathrm{BFO}}(t - t_{\mathrm{delay}})) \\ + \cos(2\pi(2 \cdot 10^9 + c_r t)(t - t_{\mathrm{delay}}) \\ - 2\pi f_{\mathrm{BFO}}(t - t_{\mathrm{delay}})). \qquad (17)$$

The output of ANT2 is amplified by the low-noise amplifier LNA1 and is then fed into mixer MXR2. The LO port of MXR2 is fed by OSC2, which has the same LO input as MXR1. The IF output of MXR2 is the product

$$\mathrm{IF}(t) = \mathrm{LO}(t) \cdot \mathrm{RX}(t).$$

As a practical consideration, the high-frequency terms can be dropped, since the IF port of MXR2 cannot output microwave frequencies. Performing the indicated multiplication in the preceding equation yields

$$\mathrm{IF}(t) = \cos[-2\pi(2 \cdot 10^9 + c_r t)t_{\mathrm{delay}} \\ + 2\pi f_{\mathrm{BFO}}(t - t_{\mathrm{delay}})] \\ + \cos[-2\pi(2 \cdot 10^9 + c_r t)t_{\mathrm{delay}} \\ - 2\pi f_{\mathrm{BFO}}(t - t_{\mathrm{delay}})]. \qquad (18)$$

As another practical consideration, the DC blocking capacitors in IF amplifier AMP1 rejects the DC phase terms, resulting in

$$\mathrm{IF}(t) = \cos(2\pi(f_{\mathrm{BFO}} - c_r t_{\mathrm{delay}})t) + \cos(2\pi(f_{\mathrm{BFO}} + c_r t_{\mathrm{delay}})t). \qquad (19)$$

Then $\mathrm{IF}(t)$ is fed into the high-Q IF filter FL1, which has center frequency f_c and bandwidth BW. Oscillator OSC1 is set to a frequency such that $f_{\mathrm{BFO}} \geq (\mathrm{BW})/(2) + f_c$, causing FL1 to pass only the lower sideband of $\mathrm{IF}(t)$. Thus the output of FL1 is

$$\mathrm{FIL}(t) = \begin{cases} \cos\left(2\pi(f_{\mathrm{BFO}} - c_r t_{\mathrm{delay}})t\right) & \text{if } \frac{-\mathrm{BW}}{2} + f_c < f_{\mathrm{BFO}} \\ & \quad -c_r t_{\mathrm{delay}} < \frac{\mathrm{BW}}{2} + f_c \\ 0 & \text{for all other values.} \end{cases} \qquad (20)$$

Only beat frequencies in the range, $(-\mathrm{BW}/2) + f_c < f_{\mathrm{BFO}} - c_r t_{\mathrm{delay}} < (\mathrm{BW}/2) + f_c$, are passed through FL1. The band-limited IF signal (which is proportional to the down-range target location) is effectively a hardware range gate, because the range to the target is directly proportional to the beat frequency $c_r t_{\mathrm{delay}}$ in an FMCW radar system.

Because increasing (decreasing) the bandwidth of FL1 increases (decreases) the range-gate duration, the range gate is adjustable if a number of different bandwidth filters are switched in and out of the IF signal chain. If f_{BFO} is increased, then FL1 passes only signals that satisfy the equality in (20). To allow the IF signals to pass through FL1, $c_r t_{\mathrm{delay}}$ would have to increase to compensate for a higher f_{BFO} frequency, because $c_r t_{\mathrm{delay}}$ is subtracted from f_{BFO}. Thus, filter FL1 will only pass beat tones further down range but at the same range duration in length, if f_{BFO} were increased. Consequently, the range gate is adjustable in physical down-range location (physical down-range time delay) by simply adjusting the frequency of f_{BFO}.

In the last step of the signal chain in Fig. 4, the output of FL1 is down-converted to base band through MXR3. The LO port of MXR3 is driven by OSC1, and the output of MXR3 is fed through Video Amp1, which has an output represented by

$$\mathrm{Video}(t) = \mathrm{BFO}(t) \cdot \mathrm{FIL}(t).$$

Video Amp1 is an active low-pass filter that rejects the higher frequency component of the cosine multiplication, resulting in the video output signal

$$\mathrm{Video}(t) = \begin{cases} \cos(2\pi c_r t_{\mathrm{delay}} t) & \text{if } \frac{-\mathrm{BW}}{2} + f_c - f_{\mathrm{BFO}} \\ & \quad < c_r t_{\mathrm{delay}} < \frac{\mathrm{BW}}{2} + f_c - f_{\mathrm{BFO}} \\ 0 & \text{for all other values} \end{cases} \qquad (21)$$

which is a range-gated base-band video signal. This result is similar to the traditional FMCW systems described in [16], [17], except that this signal is band limited by a high-Q band-pass filter that provides a short-duration range gate for the long duration LFM chirp waveforms produced by this radar system. This radar is capable of chirping from 1.926 GHz to 4.069 GHz in 2.5 ms, 5 ms, and 10 ms providing chirp rates (c_r) of 857 GHz/s, 428 GHz/s, and 214 GHz/s respectively. The narrow IF bandwidth provides a range gate of 8.75 ns for a chirp rate of 857 GHz/s, 17.5 ns for a chirp rate of 428 GHz/s, and 35 ns for a chirp rate of 214 GHz/s. This range gate rejects the flash off of the air-slab boundary, allowing full dynamic range of the digitizer to be applied to the target scene behind the air-slab boundary.

The hardware implementation is much like that of [17], where the radar sensor is moved automatically down a 2.44 m linear rail to acquire range profiles of the target scene at 5.08 cm evenly spaced increments. A photograph of the radar system is shown
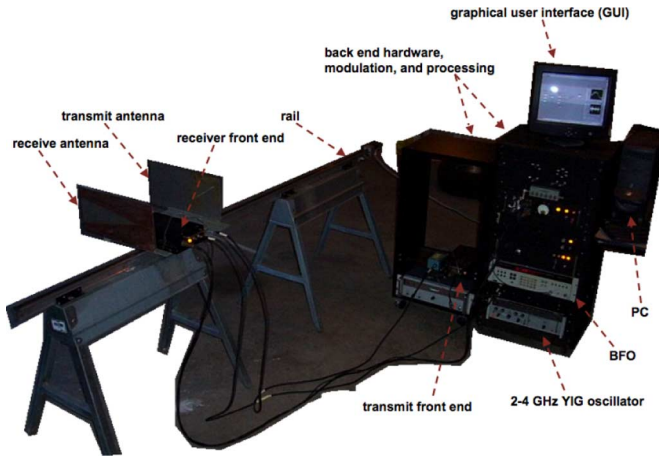
Fig. 5. The S-band through-slab radar imaging system.

Fig. 6. Target scene of 15.24 cm tall 0.95 cm diameter carriage bolts in a block 'S' pattern.

in Fig. 5. The receiver noise figure (NF) is 3.3 dB, the minimum detectable signal (MDS) was measured to be less than -125 dBm, and the system analog dynamic range was measured to be greater than 120 dB (before pulse compression). The peak transmit power is approximately 10 mW and is adjustable down to the pW level. The transmit and receive antennas are linearly tapered slot antennas ([19]). Further details are presented in [20].

Calibration is achieved by acquiring a single range profile of a 1.5 m tall metal pole at a known location down range. This pole is assumed to be a point target. Calibration coefficients are applied to all range profiles prior to SAR processing. Coherent background subtraction is utilized in all data shown.

The transmit pulse is continuously correlated with the received pulses in MXR2, the output of Video Amp1 is digitized, and the IDFT is applied to this data to determine range. This technique is known as stretch mode pulse compression processing [21]. By using a 200 KSPS 16 bit ADC, this radar is capable of ranging targets from 0–70 m down-range alias-free with a 10 ms pulse that chirps across 2.14 GHz of bandwidth. This architecture provides an equivalent 467 ps radar pulse resulting in a 7 cm range resolution, but at the same time, is as sensitive as a receiver with a 100 Hz bandwidth [22]. An equivalent UWB impulse radar architecture would transmit a 467 ps short pulse and would have to acquire the entire instantaneous bandwidth of this pulse scattered off of the target scene, requiring an ADC with 2.14 GHz of bandwidth and a sampling rate of at least 4.28 GSPS. Both architectures would provide the same range resolution; however, a 4.28 GSPS ADC is generally more expensive than a 200 KSPS ADC utilized in the modified FMCW radar architecture.

Furthermore, the average power transmitted by the modified FMCW architecture is 2 mW, where the peak power is 10 mW with a 10 ms pulse width and a PRF of approximately 20 Hz (a PRF of 90 Hz should be possible with better data acquisition equipment). An equivalent 2 mW average power UWB short-pulse radar would have to transmit 2 watts of peak power at a high PRF of 2.14 MHz to achieve an alias-free maximum range of 70 m. This radar would have to integrate approximately 21 400 pulses coherently to achieve the same SNR as one 10 ms pulse from the modified FMCW radar. In addition to this, 2 watt power amplifiers covering 2–4 GHz are generally more expensive than 10 mW power amplifiers.

V. FREE-SPACE RADAR IMAGERY

In this section, free-space imagery is discussed for selected scenarios to test the SAR's sensitivity and resolution. Although the radar was exercised for target scenes with numerous objects, only the free-space images of a block-S configuration of 14 carriage bolts, with equal spacing of approximately 0.305 m between adjacent bolts, are discussed (Fig. 6). The bolts are mounted on a styrofoam board ($\epsilon_r = 1.03$ [14]) that is parallel to the ground and 3.7 m from the rail SAR. Furthermore, the board is essentially electromagnetically transparent at the SARs transmission frequencies (1.926–4.069 GHz). Each bolt is 15.24 cm long with a diameter of 0.95 cm. Each bolt is mounted vertically as shown in Fig. 6 providing small down range and cross range extents, allowing the bolts act like a point scatterers. Imaging these bolts allows the SAR's resolution to be tested.

The range resolution was measured by irradiating the target scene with 10 mW of peak transmit power resulting in the image shown in Fig. 7(a). The expected range resolution (without weighting) depends on the chirp bandwidth, and was calculated using the equation [15]

$$\rho_r = \frac{c}{2B} \quad (22)$$

where B is the chirp bandwidth ($= 2.143$ GHz), resulting in $\rho_r = 7$ cm. The measured down-range resolution is 8.8 cm, showing that the SAR is performing close to what theory predicts.

The cross range resolution depends on the length of the array L ($= 2.44$ m) and the distance of the point target to the front of the array in both down range and cross range. This is calculated (without weighting) by using [15]

$$\rho_{cr} = \frac{\lambda R_t}{2L \sin \phi_{dc} \cos (\Delta \theta / 2)} \quad (23)$$

where R_t is the range to point target, ϕ_{dc} is the angle from the center of the aperture to the point target, and $\Delta \theta$ is the change in target aspect angle from 0 to L across the aperture. The expected cross range resolution for all targets shown at 4.87 m down range is 10.4 cm. The measured cross range is 11.7 cm. The expected
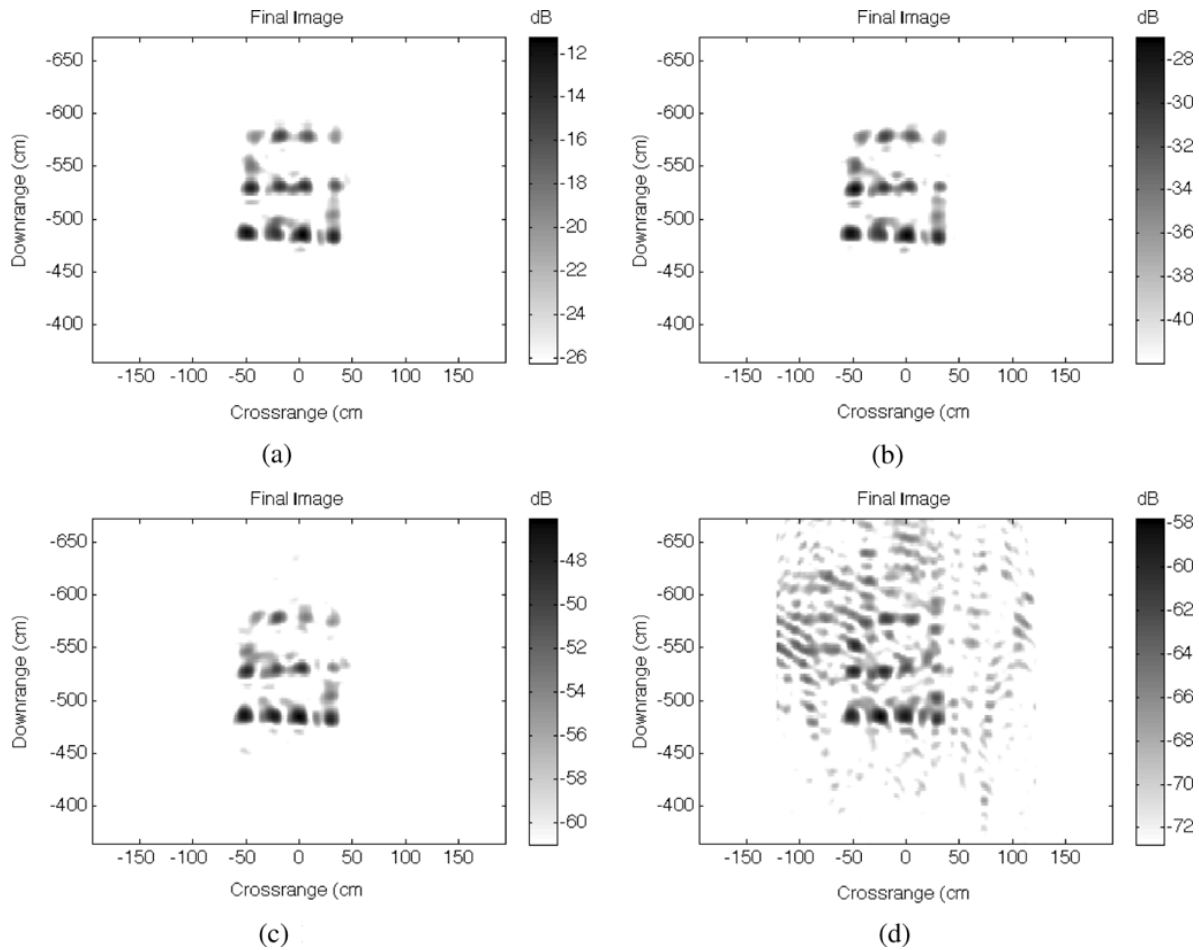
Fig. 7.   SAR image of a group of carriage bolts in free-space using 10 mW (a), 10 nW (b), 100 pW (c), and 5 pW (d) of transmit power.

cross range resolution for all targets shown at 5.76 m is 12.2 cm. The measured cross range is 11.9 cm. These results show that the SAR is performing close to predictions.

To test the SAR's sensitivity, the configuration was irradiated at three extremely low power levels at the antenna terminals [10 nW, 100 pW, 5 pW peak power measured images shown in Fig. 7(b)–(d)]. On comparing the imagery at these power levels to the imagery at the full-power setting (10 mW), the authors observed that the apparent image signal-to-noise ratios and resolution for every power level were nearly identical, except for the 5 pW case where the point targets furthest down range are fading into the noise. This near equivalence indicates that the high sensitivity of this radar architecture is effective for low-power free-space imaging. At the high-power setting, the image is a reasonably clear rendition of the actual configuration [Fig. 7(a)] One can discern the 14-bolt pattern as the 14 fuzzy rectangles in a block-S configuration. In the interest of comparison, Fig. 7(d) displays the image at the lowest power level (5 pW), with 64 coherent integrations or less per range profile. Coherent integration is required to increase the SNR for measurements at this power level. While the bolts near the top of the block-S appear to be fading into the noise, each bolt is clearly shown in the image. By visually inspecting Fig. 7(a)–(d), one can estimate the down-range and cross-range extents. In particular, the down-range extent is 0.89 m between 4.87 m and 5.76 m, and

the cross-range extent is 1 m between −0.5 m and 0.5 m. The bolts are not as well separated in the cross-range dimension as they are in the down-range dimension because the down-range resolution is better than the cross-range resolution. A highly sensitive system like this SAR could have numerous applications, including RCS measurement, automotive radar, and low probability of detection radar.

VI.   THROUGH-SLAB SAR IMAGERY

To conduct through-slab imaging, a lossy dielectric slab was built out of solid concrete blocks that were mortared together. The resulting slab was approximately 10 cm thick, 3 m wide, and 2.4 m tall. The slab was built onto a wood structure with casters so that the ensemble could be repositioned within the laboratory space (inside a garage). A photograph of the target scene, showing the rail SAR positioned 9 m from the slab in the garage, is displayed in Fig. 8. The dielectric properties of this slab are difficult to define because they depend on the mixture of the concrete used in the blocks. Consequently, based on the work of Halabe *et al.* [13], the relative permittivity (ϵ_r) and the conductivity (σ) of the slab are assumed to be 5 and varying linearly from 0.140–0.188 S/m across the transmit chirp frequency range of 1.929–4.069 GHz. These dielectric properties are presented here as a reference and were not used in the imaging algorithm or to focus the resulting imagery.
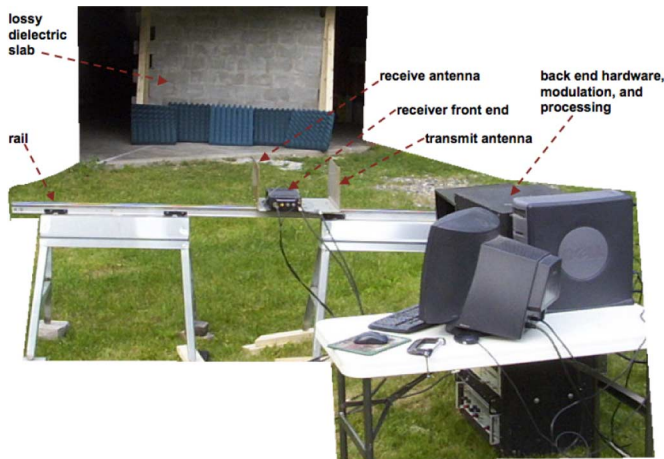
Fig. 8. Through-lossy-dielectric slab image scene where the S-band rail SAR is located 9 m from the slab.

Measured images of objects behind the slab were achieved using 10 mW of peak transmit power and 32 (or less) coherent integrations per range profile. All targets imaged were made up of good electric conductors. For the purpose of comparison to the measured imagery, the simulated imagery was calculated from the model in Section III. All imagery is based on the object scene depicted in Fig. 1, where the distances $\{d_1, d_3, d_4\}$ are taken to be $\{9 \text{ m}, 11.4 \text{ m}, 0.34 \text{ m}\}$. When the hidden object is a cylinder of radius 7.62 cm, the simulated and measured images are in close agreement (Fig. 9). The additional features in the measured image are probably induced by interactions between the cylinder and the (subtracted) background clutter.

For a second scene, three objects (the carriage bolts of Fig. 6) having much smaller RCSs than the cylinder are placed along a diagonal line behind the slab. These bolts are mounted vertically, providing small down range and cross range extents that allow the bolts to act like point scatterers, hence enabling the SAR's resolution through a lossy dielectric to be tested. In the image (Fig. 10), the location of each bolt is clearly discernible. The fact that this group of bolts can be imaged demonstrates the SAR's sensitivity when imaging through a lossy dielectric slab. These results show the potential for imaging other low RCS targets behind a slab, including objects made out of dielectrics. The dielectric objcts would have to scatter an RCS equal to or greater than a 15.24 cm tall metal bolt. The expected down range resolution, calculated from (22) is 7 cm. The measured down range resolution is 8.9 cm and 7.8 cm for the bolts located at 1114 cm and 1205 cm down range, respectively. The expected cross range resolutions calculated from (23) are 23.1 cm and 24.9 cm at 1114 cm and 1205 cm down range, respectively. The measured cross range resolutions are approximately 21.5 cm and 32.2 cm at 1114 cm and 1205 cm down range. When imaging through a lossy dielectric slab, the range resolution is very close to what is possible in free-space. Consequently, such a radar system could be useful in imaging diverse object scenes behind dielectric slabs, when little *a priori* knowledge of the obscured objects is available.
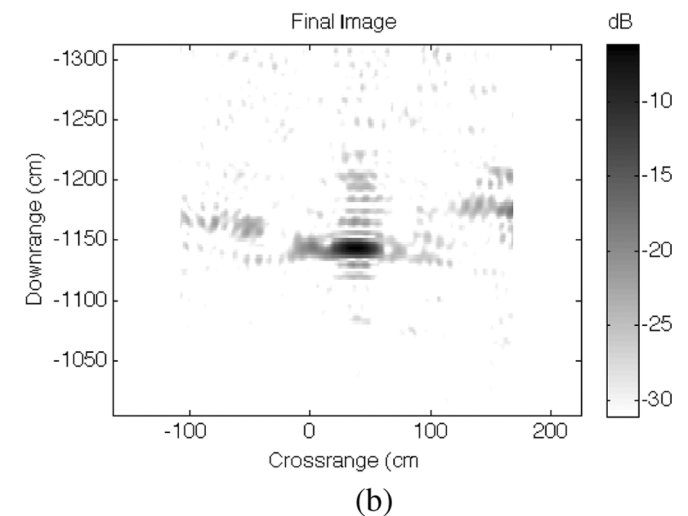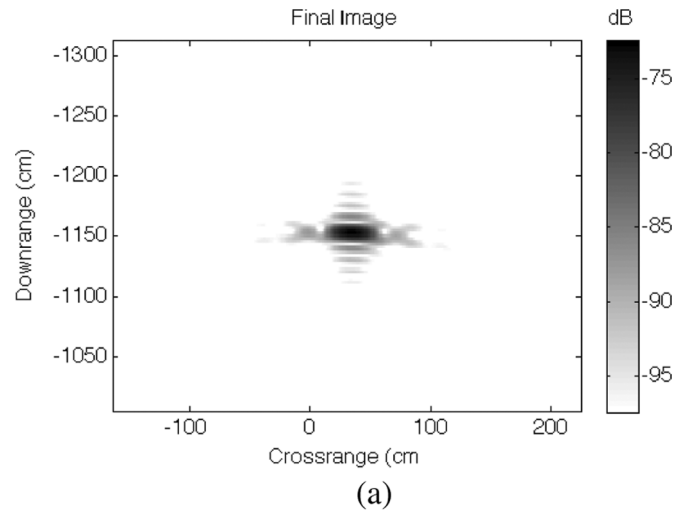

(a)

(b)

Fig. 9. SAR image of an $a = 7.62$ cm radius cylinder behind a 10 cm thick lossy-dielectric slab simulated (a) and measured (b).
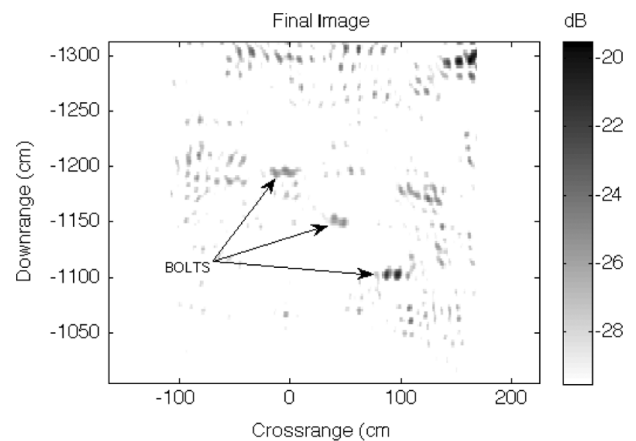

Fig. 10. Diagonal row of three 15.24 cm tall 0.95 cm diameter carriage bolts imaged behind a 10 cm thick lossy-dielectric slab.

VII. Conclusion

A LFM radar solution to through-slab imaging was chosen because of the single-pulse sensitivity and dynamic range

achievable by pulse compression of long duration pulses. Due to the small imaging geometry of practical through-slab scenarios, an FMCW radar mode had to be utilized. It was shown by simulation that the scattered field due to the air-slab boundary dominates the single-pulse scattered return from the target scene. It was also shown that the return from a target behind a lossy slab is significantly lower than in free space. It was determined that, due to the large scattered signal from the air-slab boundary, a modified FMCW architecture had to be developed that is capable of range-gating out the scattered return from the air-slab boundary, allowing low RCS target scenes to be imaged through a lossy-dielectric slab with nearly perfect resolution. In addition, low RCS target scenes in free-space could be SAR imaged at low transmit power, down to 5 pico-watts. This radar sensor is effective at SAR imaging small targets behind a lossy dielectric slab at stand-off ranges using low amounts of transmit power (10 milli-watts peak) and utilizing easy-to-meet ADC specifications (16 bits at 200 KSPS). Future work will include the real-time implementation of this SAR sensor on a multiple-input multiple-output (MIMO) antenna array.

REFERENCES

[1] M. A. Barnes, S. Nag, and T. Payment, "Covert situational awareness with handheld ultra-wideband short pulse radar," in *Proc. Radar Sensor Technology VI, SPIE*, 2001, vol. 4374.

[2] S. Nag, M. A. Barnes, T. Payment, and G. W. Holladay, "An ultra-wideband through-wall radar for detecting the motion of people in real time," in *Proc. Radar Sensor Technology and Data Visualization, PSPIE*, 2002, vol. 4744.

[3] R. Benjamin, I. J. Craddock, E. McCutcheon, and R. Nilavalan, "Through-wall imaging using real-aperture radar," in *Proc. Sensors, and Command, Control, Communications, and Intelligence (C3I) Technologies for Homeland Security and Homeland Defense IV*, May 20, 2005, vol. 5778.

[4] A. Berri and R. Daisy, "High-resolution through-wall imaging," in *Proc. Sensors, and Command, Control, Communications, and Intelligence (C3I) Technologies for Homeland Security and Homeland Defense V, SPIE*, 2006, vol. 6201, no. 201J.

[5] W. Zhiguo, L. Xi, and F. Yuanchun, "Moving target position with through-wall radar," presented at the CIE'06 Int. Conf. on Radar, Oct. 2006.

[6] F. Ahmad, M. G. Amin, S. A. Kassam, and G. J. Frazer, "A wideband, synthetic aperture beamformer for through-the-wall imaging," in *Proc. IEEE Int. Symp. on Phased Array Systems and Technology*, Oct. 14–17, 2003, pp. 187–192.

[7] F. Ahmad, M. G. Amin, and S. A. Kassam, "Through-the-wall wideband synthetic aperture beamformer," in *Proc. IEEE Antennas and Propagation Society Int. Symp.*, Jun. 20–25, 2004, vol. 3, pp. 3059–3062.

[8] F. Ahmad, M. G. Amin, and S. A. Kassam, "Synthetic aperture beam-former for imaging through a dielectric wall," *IEEE Trans. Aerosp. Electron. Syst.*, vol. 41, no. 1, pp. 271–283, Jan. 2005.

[9] M. Lin, Z. Zhongzhao, and T. Xuezhi, "A novel through-wall imaging method using ultra wideband pulse system," in *Proc. IIH-MSP'06 Int. Conf. on Intelligent Information Hiding and Multimedia Signal Processing*, Dec. 2006, pp. 147–150.

[10] M. Dehmollaian and K. Sarabandi, "Refocusing through building walls using synthetic aperture radar," *IEEE Trans. Geosci. Remote Sensing*, vol. 46, no. 6, pp. 1589–1599, Jun. 2008.

[11] M. G. Amin and F. Ahmad, "Wideband synthetic aperture beam-forming for through-the-wall imaging," *IEEE Signal Processing Mag.*, pp. 110–113, Jul. 2008.

[12] R. E. Collin, *Field Theory of Guided Waves*, 2nd ed. Piscataway, NJ: IEEE Press, 1991.

[13] U. B. Halabe, K. Maser, and E. Kausel, "Propagation characteristics of electromagnetic waves in concrete," Massachusetts Institute of Technol. Cambridge Dept. Civil Eng., Tech. Rep. AD-A207387, Mar. 1989.

[14] C. A. Balanis, *Advanced Engineering Electromagnetics*. New York: Wiley, 1989.

[15] W. G. Carrara, R. S. Goodman, and R. M. Majewski, *Spotlight Synthetic Aperture Radar Signal Processing Algorithms*. Boston, MA: Artech House, 1995.

[16] A. G. Stove, "Linear FMCW radar techniques," *Proc. Inst. Elect. Eng. Radar and Signal Processing*, vol. 139, pp. 343–350, Oct. 1992.

[17] G. L. Charvat, "Low-cost high resolution X-band laboratory radar system for synthetic aperture radar applications," presented at the Antenna Measurement Techniques Association Conf., Austin, Texas, Oct. 22–27, 2006.

[18] The American Radio Relay League, Inc71st ed. Newington, CT, 1994, The ARRL Handbook.

[19] R. Janaswamy, D. H. Schaubert, and D. M. Pozar, "Analysis of the transverse electromagnetic mode linearly tapered slot antenna," *Radio Sci.*, vol. 21, no. 5, pp. 797–804, Sep.–Oct. 1986.

[20] G. L. Charvat, "A Low-Power Radar Imaging System," Ph.D. dissertation, Dept. Elect. Comput. Eng., Michigan State Univ., East Lansing, MI, 2007.

[21] M. I. Skolnik, *Introduction to Radar Systems*. New York, NY: McGraw-Hill, 1962.

[22] B. L. Lewis, F. F. Kretschmer Jr, and W. W. Shelton, *Aspects of Radar Signal Processing*. Norwood, MA: Artech House, 1986.

[23] G. L. Charvat, L. C. Kempel, and C. Coleman, "A low-power high-sensitivity X-band rail SAR imaging system," *IEEE Antennas Propag. Mag.*, pp. 108–115, Jun. 2008.

[24] U. L. Rhode, J. Whitaker, and T. T. N. Bucher, *Communications Receivers*, 2nd ed. New York, NY: McGraw-Hill, 1996.

Gregory L. Charvat (M'09) was born in Lansing, MI, on March 14, 1980. He received the B.S.E.E., M.S.E.E., and Ph.D. degree electrical engineering from Michigan State University, East Lansing, in 2002, 2003, and 2007 respectively.

He is currently a technical staff member at Lincoln Laboratory, Massachusetts Institute of Technology, Lexington, since September of 2007. He has authored or coauthored four journal articles and 18 conference papers on various topics including; applied electromagnetics, synthetic aperture radar (SAR), and phased array radar systems. He has developed four rail SAR imaging sensors, one MIMO phased array radar system, an impulse radar, and holds a patent on a harmonic radar remote sensing system.

Dr. Charvat is currently serving as the publications and poster session Co-Chair on the IEEE Phased Array 2010 committee and as Chair of the IEEE AP-S Boston Chapter.

Leo C. Kempel (F'09) received the B.S.E.E. degree from the University of Cincinnati, OH, in 1989 and the M.S.E.E. and Ph.D. degrees from Michigan State University, East Lansing, in 1990 and 1994, respectively.

During his undergraduate studies, he participated in the Cooperative Education Program at General Dynamics Ft. Worth Division. After completion of his undergraduate degree, he joined the Radiation Laboratory, University of Michigan, where he studied electromagnetic theory and computational electromagnetics. After a brief Postdoctoral research experience at UM, he joined Mission Research Corporation in Valparaiso, FL. He has led several funded research efforts in the general areas of computational electromagnetics, antenna design, scattering analysis, and high power/ultrawideband microwaves. During this time, he coauthored a textbook on the use of finite element methods in electromagnetics. In August 1998, he joined the Department of Electrical and Computer Engineering, Michigan State University, East Lansing.

Edward J. Rothwell (F'05) was born in Grand Rapids, MI, on September 8, 1957. He received the B.S. degree in electrical engineering from Michigan Technological University, Houghton, in 1979, the M.S. degree in electrical engineering and the degree of electrical engineer from Stanford University, Stanford, CA, in 1980 and 1982, and the Ph.D. degree in electrical engineering from Michigan State University, East Lansing, MI, in 1985, where he held the Dean's Distinguished Fellowship.

He worked for Raytheon Co., Microwave and Power Tube Division, Waltham, MA, from 1979 to 1982, on low power traveling wave tubes, and for MIT Lincoln Laboratory, Lexington, MA, in 1985. He has been at Michigan State University from 1985 to 1990 as an Assistant Professor of electrical engineering, from 1990 to 1998, as an Associate Professor, and from 1998 as Professor. He is coauthor of the book *Electromagnetics* (Boca Raton, FL: CRC Press, 2001; 2nd edition 2008).

Dr. Rothwell is a Fellow of the IEEE, and is a member of Phi Kappa Phi, Sigma Xi, and Commission B of URSI. He received the John D. Withrow award for teaching excellence from the College of Engineering at Michigan State University in 1991, 1996 and 2006, the Withrow Distinguished Scholar Award in 2007, and the MSU Alumni Club of Mid Michigan Quality in Undergraduate Teaching Award in 2003. He was a joint recipient of the Best Technical Paper Award at the 2003 Antenna Measurement Techniques Association Symposium, and in 2005 he received the Southeast Michigan IEEE Section Award for Most Outstanding Professional.
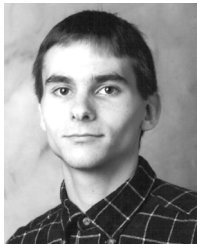
Christopher M. Coleman (M'02) received the B.S., M.S., and Ph.D. degrees in electrical engineering from Michigan State University, East Lansing, in 1996, 1999, and 2002, respectively.

Since 2007, he has been with Integrity Applications Incorporated, Chantilly, VA. His research interests include self-structuring antennas, synthetic aperture radar, and radar cross-section measurement techniques.

Eric L. Mokole (SM'01) received the B.S. degree in applied mathematics from New York University, New York, NY, in 1971, the M.S. degree in mathematics from Northern Illinois University, DeKalb, in 1973, dual M.S. degrees in physics and applied mathematics from the Georgia Institute of Technology, Atlanta, in 1976 and 1978, respectively, and the Ph.D. degree in mathematics from the Georgia Institute of Technology, in 1982.

For the 1982 to 1983 academic year, he was an Assistant Professor of mathematics at Kennesaw College, Kennesaw, GA. From 1983 to 1986, he held a position in the Electronic Warfare Division of the Naval Intelligence Support Center (now the Office of Naval Intelligence) in Washington DC. Since 1986, he has been employed by the Radar Division of the Naval Research Laboratory (NRL), Washington DC. From February 2001 through August 2005, he was Head of the Surveillance Technology Branch, where he supervised approximately 30 R&D scientists, engineers, and mathematicians. His duties included: providing innovative technical solutions to Navy radar problems; developing new radar concepts, signal-processing/detection techniques, and electromagnetics research concepts; directing teams of researchers to pursue R&D solutions; and conducting basic and applied research. He led efforts on space radar (trans-ionospheric propagation), ultrawideband radar (antennas, propagation, mine detection, sea scatter, impulse radar), and waveform diversity (spectrally clean waveforms). From September of 2005 until February of 2008, he was the Acting Superintendent of the Radar Division, after which he resumed his role as Head of the Surveillance Technology Branch. As Acting Superintendent, he managed a 120-person research group, directed the R&D thrust of the Radar Division, and conducted R&D on radar-related topics. He has over 70 conference publications, journal articles, book chapters, and reports and is the lead Editor of *Ultra-Wideband, Short-Pulse Electromagnetics 6* (Kluwer Academic/Plenum Publishing, 2003), co-editor of *Ultra-Wideband, Short-Pulse Electromagnetics 7* (Kluwer Academic/Plenum Publishing, 2007), and co-author of *Physics of Multiantenna Systems and Broadband Processing* (Wiley, 2008)

Dr. Mokole is a member of five IEEE Societies (AP, MTT, EMC, AES, GRS), the American Geophysical Union, the American Mathematical Society, the American Physical Society, and the Society for Industrial and Applied Mathematics. In addition, he is a Senior Member of the IEEE, the Navy lead of the Program Committee for the Tri-Service Radar Symposia, a member of the High-Power Electromagnetics Committee, a member of the IEEE AES Radar Systems Panel, the Vice Chair of NATOs Sensors and Electronics Technology Panel, a government liaison to USNC-URSI, and a founding member of the Tri-Service Waveform Diversity Working Group.